Biochemical and Biophysical Research Communications 443 (2014) 470–476

Contents lists available at ScienceDirect

Biochemical and Biophysical Research Communications

journal homepage: www.elsevier.com/locate/ybbrc

Accumulation of nano-sized particles in a murine model of angiogenesis

Thomas R. Wittenborn [a,*,1], Esben K.U. Larsen [b,c,d,1], Thomas Nielsen [a,b], Louise M. Rydtoft [e], Line Hansen [b,c,d], Jens V. Nygaard [b,f], Thomas Vorup-Jensen [d,g], Jørgen Kjems [b,c,d], Michael R. Horsman [a], Niels Chr. Nielsen [b,d,h]

[a] Department of Experimental Clinical Oncology, Aarhus University Hospital, Noerrebrogade 44, 8000 Aarhus C, Denmark
[b] Interdisciplinary Nanoscience Center (iNANO), Aarhus University, Gustav Wieds Vej 14, 8000 Aarhus C, Denmark
[c] Department of Molecular Biology and Genetics, Aarhus University, C.F. Moellers Allé 3, 8000 Aarhus C, Denmark
[d] The Lundbeck Foundation Nanomedicine Center for Individualized Management of Tissue Damage and Regeneration (LUNA), Aarhus University, Aarhus, Denmark
[e] Center of Functionally Integrative Neuroscience (CFIN), Aarhus University Hospital, Noerrebrogade 44, 8000 Aarhus C, Denmark
[f] Department of Engineering, Aarhus University, Finlandsgade 22, 8000 Aarhus, Denmark
[g] Department of Biomedicine, Aarhus University, Bartholins Allé 6, 8000 Aarhus, Denmark
[h] Center for Insoluble Protein Structures (inSPIN) and Department of Chemistry, Aarhus University, Gustav Wieds Vej 14, 8000 Aarhus C, Denmark

ARTICLE INFO

Article history:
Received 22 November 2013
Available online 7 December 2013

Keywords:
Angiogenesis
Iron oxide particles
Ultrahigh-field MRI
Sponge model

ABSTRACT

Purpose: To evaluate the ability of nm-scaled iron oxide particles conjugated with Azure A, a classic histological dye, to accumulate in areas of angiogenesis in a recently developed murine angiogenesis model.
Materials and methods: We characterised the Azure A particles with regard to their hydrodynamic size, zeta potential, and blood circulation half-life. The particles were then investigated by Magnetic Resonance Imaging (MRI) in a recently developed murine angiogenesis model along with reference particles (Ferumoxtran-10) and saline injections.
Results: The Azure A particles had a mean hydrodynamic diameter of 51.8 ± 43.2 nm, a zeta potential of −17.2 ± 2.8 mV, and a blood circulation half-life of 127.8 ± 74.7 min. Comparison of MR images taken pre- and 24-h post-injection revealed a significant increase in R_2^* relaxation rates for both Azure A and Ferumoxtran-10 particles. No significant difference was found for the saline injections. The relative increase was calculated for the three groups, and showed a significant difference between the saline group and the Azure A group, and between the saline group and the Ferumoxtran-10 group. However, no significant difference was found between the two particle groups.
Conclusion: Ultrahigh-field MRI revealed localisation of both types of iron oxide particles to areas of neovasculature. However, the Azure A particles did not show any enhanced accumulation relative to Ferumoxtran-10, suggesting the accumulation in both cases to be passive.
© 2013 Elsevier Inc. All rights reserved.

1. Introduction

Angiogenesis has been established as a common feature of many pathological conditions including diseases such as atherosclerosis and cancer [1,2]. During the angiogenetic process and in the initial phase of neovascular maturation, the vessels tend to be fragile and leaky because of a discontinuous or missing basal membrane [3,4]. These leaky vessels introduce a potential route of transport from the blood into the extravascular extracellular space (EES) and extracellular matrix (ECM) [5–7]. The ECM contains an abundance of heavily glycosylated proteins, in particular sulphated glycosaminoglycans [8], which under physiological conditions are negatively charged.

These combined features can be exploited for drug delivery or imaging [5–7,9], and has made angiogenesis a desired target for new nanotechnological approaches. The field of nanotechnology has expanded markedly within the past decades and has now developed to such an extent that it has become possible to manufacture tailor-made nm-scaled particles to target specific biomarkers of biological processes [10–15].

Azure A, a small positively charged metachromatic dye used for decades in histology [16], has been known to stain DNA, azurophilic granules of leukocytes, and other negatively charged molecules [17–20]. By conjugating this small dye to a nano-sized particle it could enable binding of the particle to the negatively charged proteoglycans in the ECM.

Here, we describe the physicochemical characterisation and accumulation properties of such an Azure A-conjugated iron oxide

* Corresponding author. Address: Department of Experimental Clinical Oncology, Aarhus University Hospital, Nørrebrogade 44, Building 5, 2nd floor, DK-8000 Aarhus C, Denmark.
E-mail address: Wittenborn@oncology.dk (T.R. Wittenborn).
[1] These authors contributed equally to this paper.

0006-291X/$ - see front matter © 2013 Elsevier Inc. All rights reserved.
http://dx.doi.org/10.1016/j.bbrc.2013.11.127

nano-sized particle. Hydrodynamic size, zeta potential, and blood circulation half-life were estimated using standard methods, and its ability to localise to areas of angiogenesis was assessed by ultrahigh-field MRI in a recently described murine angiogenesis model [21].

2. Materials and methods

2.1. Materials

Diethyl ether, 3-Amino-7-(dimethylamino)-phenothiazin-5-ium (Azure A) and (3-Amino-propyl)-triethoxysilane (Si-NH_2) were purchased from Sigma–Aldrich, St. Louis, MO, USA. NHS-PEG-Maleimide (PEG molecular weight of 2000 Da) was purchased from IRIS biotech GmbH, Marktredwitz, Germany. Methoxy PEG succinimidyl active ester (NHS-PEG; PEG molecular weight of 2000 Da) was purchased from Rapp-polymere GmbH.

2.2. Synthesis of Azure A conjugated nano-sized particles

The synthesis of oleic acid-coated iron oxide particles is described by Larsen et al. [7]. Iron oxide particles (50 mg) coated with oleic acid were dissolved in 5 mL toluene. Under constant stirring, 10 μL Si-NH_2 (55.8 μmol), 38 mg NHS-PEG (50.7 μmol), 0.8 mL triethylamine (TEA) and 80 μL H_2O were added. After overnight reaction particles were heated to 105 °C for 1 h and washed in toluene/pentane three times. To conjugate Azure A, 15 mg particles were first conjugated to 90 mg NHS-PEG-Maleimide (45 μmol) and reacted together with 90 μL DIC (714 μmol) and 200 μL TEA in toluene for 24 h. Particles were washed in toluene/pentane three times. Then 9 mg Azure A was added to the particle formulations in 1 mL DMSO with 60 μL TEA for 24 h. Finally, the particles were precipitated with diethyl ether. Particles were purified by dialysis (6–8 kDa cut-off) against PBS for 5 days, changing the solute twice a day. Following dialysis the particles were centrifuged to remove aggregates.

2.3. Characterisation of functionalized particles

The hydrodynamic size and zeta potential of the Azure A particles were assessed by dynamic light scattering (DLS) using a Zetasizer Nano ZS (Malvern Instruments, Malvern, UK). Measurements were made in phosphate buffered solution at pH 7.0 and 25 °C. Three consecutive measurements were performed and the mean ± standard deviation was calculated.

To determine blood circulation half-life, particles were diluted in saline and injected intravenously (i.v.) into male CDF1 mice. Three mice were injected with the Azure A particle formulation and six mice were injected with the Ferumoxtran-10 formulation. A volume of 10 μL/g of mouse body weight was administered at a dose of 5 mg Fe/kg. A control group with three mice received i.v. saline injections also in a volume of 10 μL/g. Blood samples were drawn from the sub-orbital sinus of animals prior to injection and 5, 60, 360 and 1440 min after injection. Blood was collected in EDTA tubes, and blood samples were centrifuged to obtain EDTA-plasma. Samples were digested using a solution of 5.5 mL Nitric acid (HNO_3) and 0.5 mL Hydrochloric acid (HCl, 12 M), which was heated to speed up the process. Iron concentrations in the samples were analysed by inductively coupled plasma atomic emission spectroscopy (ICP-AES) using a Plasma 2000 (Perkin-Elmer, USA) as described elsewhere [22]. Blood circulation half-life was calculated based on linear regression of the exponential washout of the injected particles.

2.4. Angiogenesis model

Fifteen male CDF1/Tac mice (12–20 weeks old) were included in the experiment. Poly-capro-lactone (PCL) discs were made in-house and prepared according to Andersen et al. [23]. The procedure for implantation of porous PCL discs has been previously described [21]. In brief, a small incision (1.5 cm) was made in the skin on the back, through which the PCL discs (measuring 8 mm in diameter and 2–3 mm in height) were subcutaneously implanted. After surgery the mice were caged individually for 3–4 weeks, which was the optimal time point after implantation for a maximum amount of neovessels [21]. Mice were distributed equally into three groups: a saline group, a reference group (Ferumoxtran-10), and an Azure A-conjugated group (Azure A).

2.5. MRI of injected particles

A 16.4 T spectroscopy/imaging system (wide-bore Bruker 700 Avance-II, Bruker Biospin, Rheinstetten, Germany) equipped with a GREAT 60 gradient system with a maximum gradient strength of 1.5T/m and a Micro 2.5 probe (coil inner diameter 25 mm) was used for the in vivo MRI. Mice were anaesthetized by intraperitoneal (i.p.) injection (10 μL/g of a mixture of 10 mg/mL ketamine and 1 mg/mL xylazin) and supplemented with top-up doses (5 μL/g) when needed. An i.p. line was connected to a syringe primed with anaesthesia to administer top-up doses. A respiration-monitoring pad was attached to the abdomen of the mice using tape and connected to a monitoring system. Mice were placed with the tissue of interest aligned to the middle of the coil. Mice were restrained using tape and the entire setup was inserted into the vertical MR scanner. Here mice were kept warm by a circulating water system around the gradients (30 °C). A pre-scan was performed and after that particles were diluted in saline and administered i.v. at a dose of 2.5 mg Fe/kg (resembling a concentration of 0.25 μg/μL injected at 10 μL/g). In the saline group, saline was administered in equal amounts (10 μL/g), and 24 h post-injection all mice were scanned again (24 h post-scan).

R_2 and R_2^* measurements were performed before and 24 h after administration of the particles using gradient echo and spin echo sequences. The measurements were performed on 10 transverse slices of 0.5 mm thickness and 0.5 mm spacing. For both gradient echo and spin echo experiments additional scanning parameters were: T_R = 4000 ms, field of view = 25 × 25 mm, acquisition matrix 256 × 192 reconstructed to 256 × 256, acquisition matrix 256 × 128 reconstructed to 256 × 256, or acquisition matrix 128 × 96 reconstructed to 128 × 128, and number of averages = 1. In the gradient echo sequence, the flip angle was 90°, and 12 T_E within the interval 3.4–58.4 ms were used, and in the spin echo sequence, 12 T_E values within the interval 8.1–117.3 ms were used.

Data analysis was performed using MATLAB 7.11 (The MathWorks, Inc., Natick, MA, USA). R_2 and R_2^* maps were produced by nonlinear least squares fitting of the image signal S for different echo times (T_Es) to the equation $S(T_E) = S(0)\exp(-T_E \cdot R_2^{(*)})$. Regions of interest (ROIs) were drawn manually on a raw image to contain the entire implanted scaffolds. From the characterisation of the angiogenesis model [21] we learned that the vasculature covered most, but not all, of the implant after 3–4 weeks. To avoid non-vascularized areas in our analysis we did the following: for the pre-scan ROIs, voxels with $R_2 < 25\ s^{-1}$ and $R_2^* < 95\ s^{-1}$ were removed for R_2 and R_2^* analysis, respectively. These values were based on the bimodal shape of the pooled ROI histograms for all the animals (Fig. 1). Because the mice were repositioned before the 24 h post-scan, and new ROIs were drawn, we assumed that the same ROI percentage was vascularised at this time point. From the post-scan ROIs we then excluded the lowest R_2 or R_2^* values leaving the same ROI voxel percentage as in the pre-scan for analysis.

Some of the obtained images suffered from water-fat shift, susceptibility or motion artefacts, resulting in poor image quality and overestimated relaxation rates. In some spin-echo images the

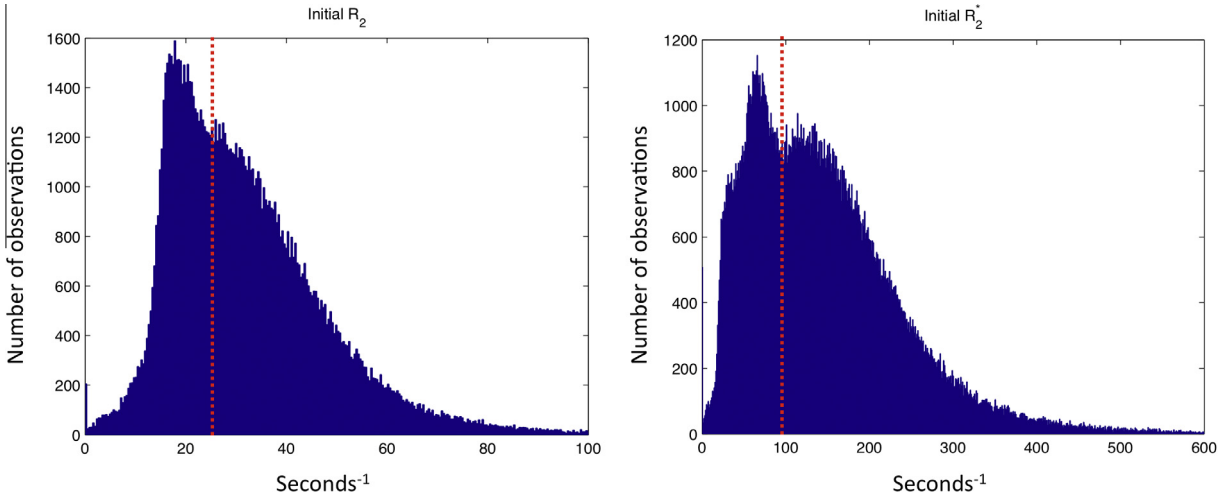

Fig. 1. Bimodal histograms of pooled voxel values. Voxel values from regions of interest from all mice in all groups were pooled into R_2 and R_2^* histograms enabling the determination of threshold values for tissue-specific areas within the implants.

water-fat-shift was problematic. These artefacts/anomalies discredited the obtained values from the maps. Hence, images were sorted in the following way: (1) Images including no or only extreme peripheral regions of the implants were excluded. (2) Images containing unnatural values for some regions in muscle tissue or bladder content were excluded; we would expect these tissues to have the same value throughout the entire structure, as their composition is uniform. The images that were left had ROIs drawn around the implants and were used in the quantitative analysis.

2.6. Statistical analysis

Data are presented as mean (±standard deviation) of individual ROI means. Comparison of relaxation rates before and after injection of the particles was evaluated using Student's *T*-test (R_2 and R_2^*). Comparison of the relative increase between the different groups was made by one-way analysis of variance (ANOVA) followed by Student's Newman–Keuls multiple comparison test using SigmaPlot version 11.0. A value of $P < 0.05$ was considered significant.

All procedures involving animal experiments were approved by the National Animal Experiments Inspectorate.

3. Results

Characterisation of the Azure A particle revealed a hydrodynamic size of 51.8 nm ± 43.2 nm, a zeta potential of −17.2 mV ± 2.8 mV, and a blood circulation half-life of 127.8 min ± 74.7 min. As comparison, Ferumoxtran-10, which has been described by Casula et al. [24], had a hydrodynamic size of 34 nm, and a zeta potential of −12.6 mV ± 1.8 mV. Blood circulation half-life was not investigated by Casula et al., but we found this to be 131.2 min ± 7.1 min.

Both particles were evaluated for angiogenesis localisation in the murine model by an ultra-high-field 16.4T spectroscopy/imaging system, and compared to saline injections. Pre- and 24 h post-injection R_2 and R_2^* maps were generated from the recorded MR-images, and regions of interest (ROIs) were drawn around the implanted scaffolds and overlaid on the raw images. A minimum threshold value was set on the pre-injection R_2 and R_2^* maps to exclude non-vascularized areas within the implants, and the same percentage amount of voxels were excluded from their post-injection R_2 and R_2^* map counterparts (Fig. 2). Remaining areas were then used to calculate mean relaxation rates of R_2 and R_2^* before and after injection of the particles (Fig. 3). R_2^* relaxation rates showed significant increase for both the Azure A particle and the Ferumoxtran-10 particle compared to pre injection. The mean R_2 relaxation rates showed a higher but non-significant increase for both particles. The relative increase was calculated for both R_2 and R_2^* relaxation rates (Fig. 4) where R_2^* relaxation rates revealed a significant increase of both the Azure A and Ferumoxtran-10 group compared to saline. When analysing the R_2 relaxation rates both particle groups had a higher but non-significant increase compared to saline.

4. Discussion

Characterising novel particles require assessment of both physicochemical and biological properties. Size, surface charge and blood circulation half-life are parameters that need to be addressed in order to give a proper evaluation of a novel particle. Particles with hydrodynamic diameters below 20–30 nm are prone to quicker excretion through the kidneys, whereas particles with a hydrodynamic diameter above 150 nm are prone to faster clearance by the reticuloendothelial system through the phagocytic uptake in liver and spleen [25–27]. Insufficient coating of particles with polyethylene glycol (PEG) can result in a high-numerical zeta potential leading to faster clearance by the reticuloendothelial system, but with a sufficiently thick coating layer the zeta potential becomes more neutral leading to less uptake of particles [28]. A long blood circulation half-life should permit sufficient time for particles to extravasate and accumulate in the areas of interest provided that the blood flow to the tissues are not compromised [10].

We attached a PEG coating to an iron oxide core in order to shield the particle from being cleared by the reticuloendothelial system. Azure A was conjugated to this particle to create a potential ECM-targeting moiety. Assessment of size, surface charge and blood circulation half-life for the Azure A particle and comparison with the well described Ferumoxtran-10, showed several similarities and indicated that the Azure A particle was not readily removed from the blood stream (blood circulation half-life of 127.8 min ± 74.7 min).

Choosing the right model for evaluating targeting potential of novel particles is very important. Tumour-associated angiogenesis models have predominantly been used to evaluate angiogenesis-

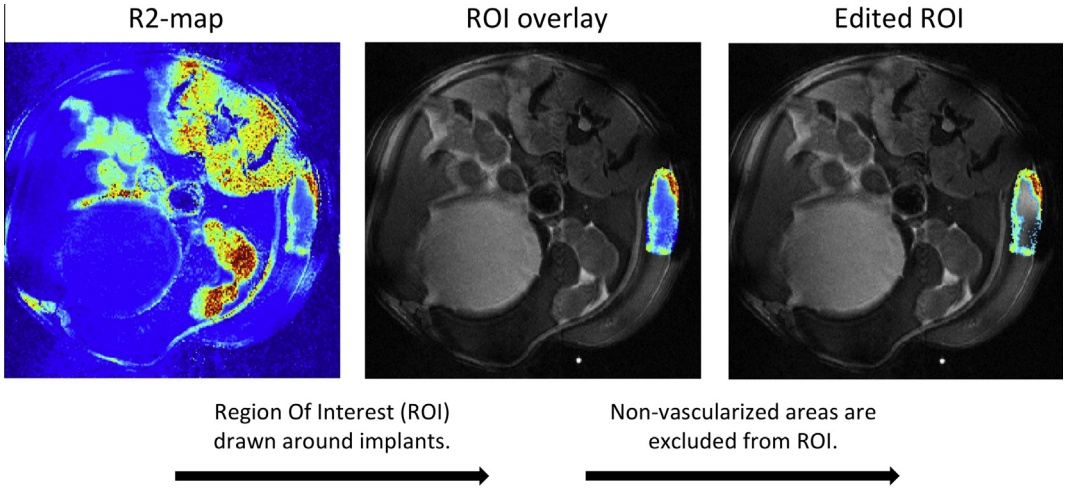

Fig. 2. Image processing from R_2 map to region of interest containing only the cellularized/vascularised implant. Regions of interest encircling the implanted scaffolds were excised from R_2 maps and overlaid on top of a raw image of the same mouse. R_2-values below a set threshold value were excluded leaving the cellularized/vascularised area of the implant for further analysis. Procedure was the same for R_2^* maps.

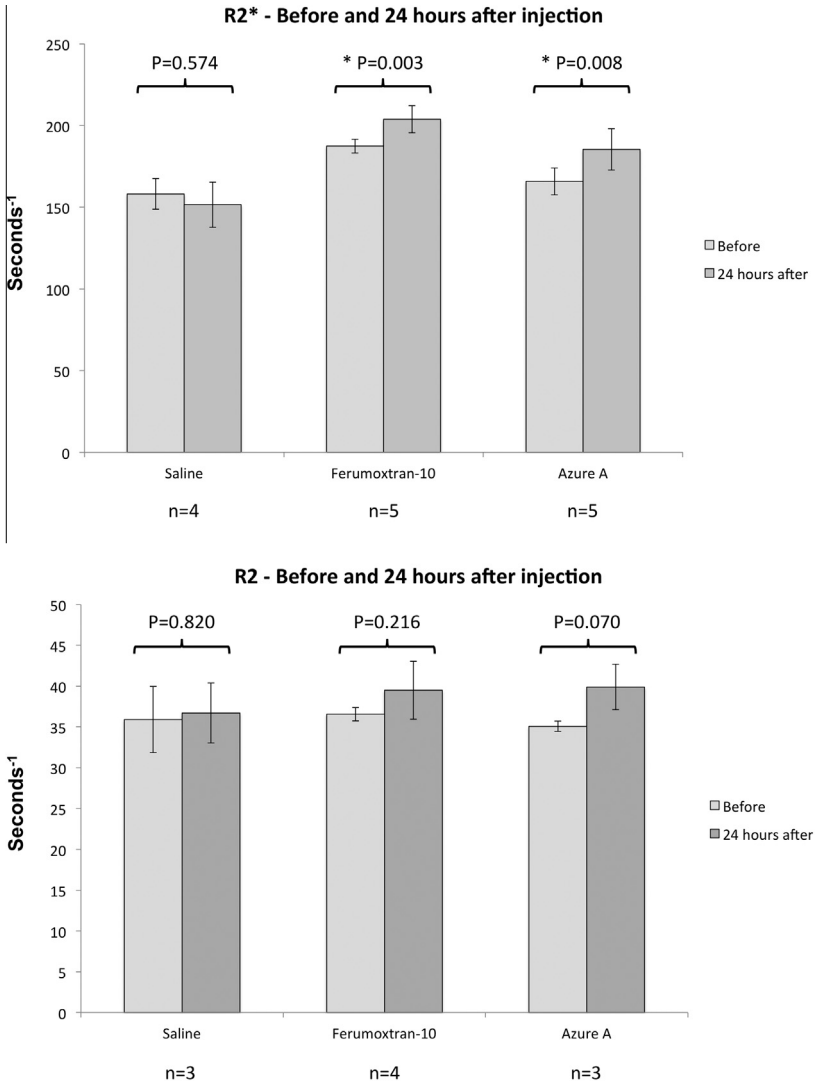

Fig. 3. Mean R_2 and R_2^* relaxation rates obtained before and after injection of iron oxide particles or saline. Error bars indicate standard deviation. Asterisks $(*)$ indicate a statistically significant difference ($P < 0.05$) between the pre-treatment and 24-h values.

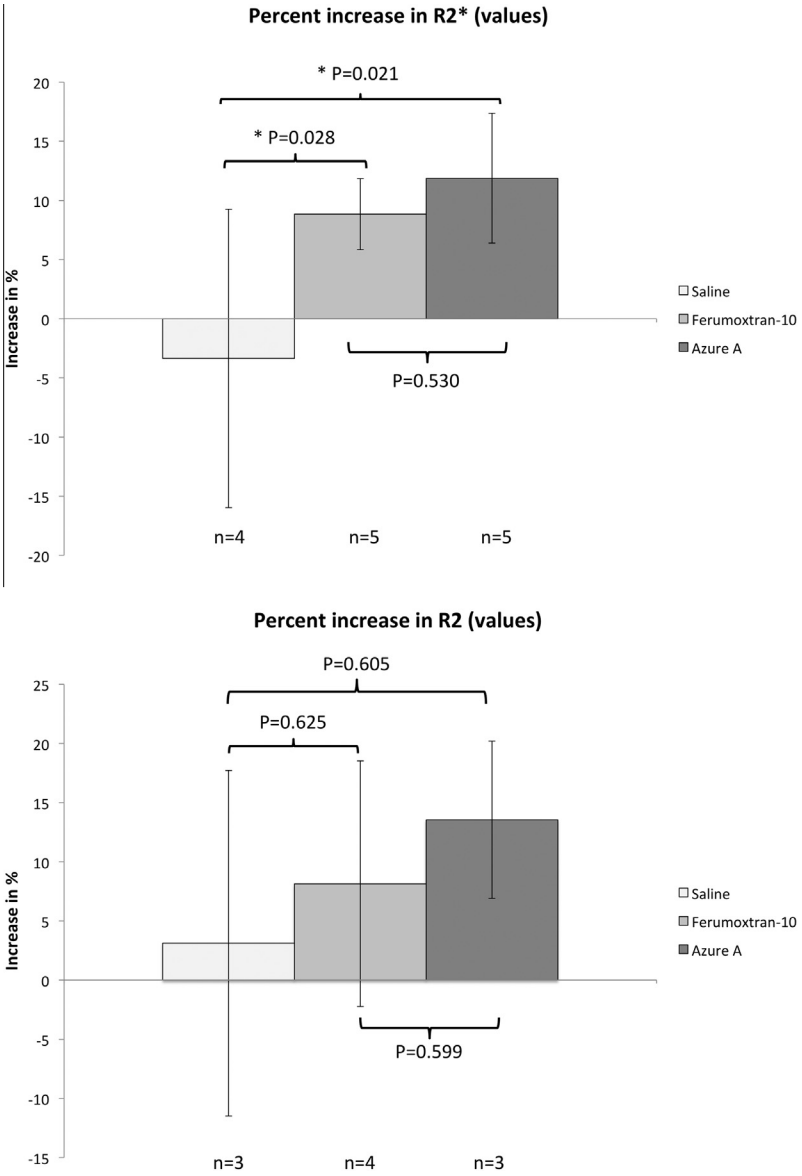

Fig. 4. Relative increase of R_2 and R_2^* for the three groups. Relative increase in R_2 and R_2^* relaxation rates were calculated. Error bars indicate standard deviation. Asterisks (∗) indicate a statistically significant difference ($P < 0.05$) between groups.

targeted nanoprobes [13,29–34].This is probably due to the extreme amount of neovessels in tumours or because cancer-treatment/diagnosis is the endpoint for the nanoprobes in question. However, the universal disease-treatment potential of these probes remain unclear as tumour-associated angiogenesis is influenced to a great extent by tumour-cells expressing extreme amounts of pro-angiogenic factors. In other words, functionalized nanoparticles identifying or targeting tumour angiogenesis will not necessarily identify or target angiogenesis associated with other diseases such as, atherosclerosis, macular degeneration, and rheumatoid arthritis. Recently, our research group developed and characterised a novel murine angiogenesis model, which was not dependent on tumour angiogenesis [21]. This model had readily identifiable and accessible areas of angiogenesis, and showed great potential for non-invasive assessment of particle efficiency.

Several points are worth noticing regarding the MRI analysis. First, the images obtained before and after particle injection have been closely co-localised so that we are looking at almost the exact same spot of the implant. This ensures that the increase seen in the implants is due to particle accumulation and not tissue-differences between before and after images. Secondly, the colour coding of the implants can be closely correlated to the amount of cell infiltration and vascularisation within each implant [21]. This means that voxels with R_2 and R_2^* values close to zero do not contain cells but only water or other fluids, whereas areas with voxel-values above threshold ($R_2 < 25\ s^{-1}$ and $R_2^* < 95\ s^{-1}$. See Fig. 1) contain both cells and vasculature.

In our analysis of the MRI data we found statistically significant differences in the R_2^* relaxation rates, but no significant differences in the R_2 relaxation rates. Although changes in the parameters R_1, R_2, and R_2^* are induced by the iron oxide particles, we would expect the effects to be more distinct in the R_2^* images. This is due to the sensitivity of R_2^* towards larger-scale field inhomogeneities created by the iron oxide core of the particles.

The increase of mean R_2 and R_2^* values was converted to percent increase, and a statistically significant difference between the saline group and the two particle groups was observed when looking at the R_2^* values. Most studies show increased accumulation of targeted versus non-targeted particles [35], which we would have expected to see when comparing the targeted

Azure A with the non-targeted Ferumoxtran-10 particle. However, as targeted particles primarily affects the uptake and internalization in cells as well as the speed of accumulation [36–38], we might have waited too long before imaging the implants after injection of the particles. If we had scanned the mice 2 h after particle injection, we might have seen a difference between the two groups. From the obtained results we have showed that iron oxide particles do accumulate in the angiogenesis model 24 h after injection, which is probably attributed to the enhanced permeability and retention effect (EPR-effect) [5,6,39].

In conclusion, we assessed hydrodynamic size, zeta potential, and blood circulation half-life of a novel Azure A-conjugated iron oxide particle, and found its biological and physicochemical properties to resemble that of the well described Ferumoxtran-10. Both of these particles were evaluated alongside saline injections in our novel angiogenesis murine model, and both showed localisation to areas of angiogenesis. However, in this particular setup we found no distinction between the two particles indicating that the observed accumulation relies primarily on the EPR-effect. Whether another setup would allow the angiogenesis model to distinguish particles from each other remains to be settled, as does the targeting ability of the Azure A particle.

Grant support

The Danish Programme Commission on Strategic Growth Technologies (NaBIIT, Grant No. 2106-05-0031); The Danish National Research Foundation; The Danish Heart Foundation (Grant No. 08-4-R64-A2037-B953-22462); The Lundbeck Foundation Center for Interventional Research in Radiation Oncology (CIRRO) and The Danish Council for Strategic Research; The Danish Cancer Society (Grant No. DP07002); National Institutes of Health (Grant No. 1R01EB012874-01). Funding sources had no involvement in study design, data collection, or analysis of results.

Disclosures

None.

Ethics

All procedures involving animal experiments were approved by the National Animal Experiments Inspectorate.

Acknowledgments

The authors would like to thank Michael Pedersen for providing the Ferumoxtran-10 particles used in the study, Inger Marie Horsman, Dorthe Grand, and Pia Schjerbeck for help and guidance with the animal experiments, and Marianne Verner Bjerre and Marianne Kristiansen for attending to the animals after surgery.

References

[1] P.R. Moreno, K.R. Purushothaman, M. Sirol, A.P. Levy, V. Fuster, Neovascularization in human atherosclerosis, Circulation 113 (2006) 2245–2252.
[2] P. Carmeliet, R.K. Jain, Angiogenesis in cancer and other diseases, Nature 407 (2000) 249–257.
[3] F.D. Kolodgie, J. Narula, C. Yuan, A.P. Burke, A.V. Finn, R. Virmani, Elimination of neoangiogenesis for plaque stabilization: is there a role for local drug therapy?, J Am. Coll. Cardiol. 49 (2007) 2093–2101.
[4] G. Bergers, L.E. Benjamin, Tumorigenesis and the angiogenic switch, Nat. Rev. Cancer 3 (2003) 401–410.
[5] A.K. Iyer, G. Khaled, J. Fang, H. Maeda, Exploiting the enhanced permeability and retention effect for tumor targeting, Drug Discov. Today 11 (2006) 812–818.
[6] K. Greish, Enhanced permeability and retention of macromolecular drugs in solid tumors: a royal gate for targeted anticancer nanomedicines, J. Drug Target. 15 (2007) 457–464.
[7] E.K.U. Larsen, T. Nielsen, T. Wittenborn, H. Birkedal, T. Vorup-Jensen, M.H. Jakobsen, L. Ostergaard, M.R. Horsman, F. Besenbacher, K.A. Howard, J. Kjems, Size-dependent accumulation of PEGylated silane-coated magnetic iron oxide nanoparticles in murine tumors, ACS Nano 3 (2009) 1947–1951.
[8] R.V. Iozzo, Matrix proteoglycans: from molecular design to cellular function, Annu. Rev. Biochem. 67 (1998) 609–652.
[9] E.K. Larsen, T. Nielsen, T. Wittenborn, L.M. Rydtoft, A.R. Lokanathan, L. Hansen, L. Ostergaard, P. Kingshott, K.A. Howard, F. Besenbacher, N.C. Nielsen, J. Kjems, Accumulation of magnetic iron oxide nanoparticles coated with variably sized polyethylene glycol in murine tumors, Nanoscale 4 (2012) 2352–2361.
[10] C. Corot, P. Robert, J.M. Idee, M. Port, Recent advances in iron oxide nanocrystal technology for medical imaging, Adv. Drug Deliv. Rev. 58 (2006) 1471–1504.
[11] D.P. Cormode, T. Skajaa, Z.A. Fayad, W.J. Mulder, Nanotechnology in medical imaging: probe design and applications, Arterioscler. Thromb. Vasc. Biol. 29 (2009) 992–1000.
[12] J.R. McCarthy, K.A. Kelly, E.Y. Sun, R. Weissleder, Targeted delivery of multifunctional magnetic nanoparticles, Nanomedicine (Lond) 2 (2007) 153–167.
[13] C.W. Kessinger, C. Khemtong, O. Togao, M. Takahashi, B.D. Sumer, J. Gao, In vivo angiogenesis imaging of solid tumors by alpha(v)beta(3)-targeted, dual-modality micellar nanoprobes, Exp. Biol. Med. (Maywood) 235 (2010) 957–965.
[14] E. Canet-Soulas, D. Letourneur, Biomarkers of atherosclerosis and the potential of MRI for the diagnosis of vulnerable plaque, MAGMA 20 (2007) 129–142.
[15] D.P. Cormode, J.C. Frias, Y. Ma, W. Chen, T. Skajaa, K. Briley-Saebo, A. Barazza, K.J. Williams, W.J. Mulder, Z.A. Fayad, E.A. Fisher, HDL as a contrast agent for medical imaging, Clin. Lipidol. 4 (2009) 493–500.
[16] H. Kramer, G.M. Windrum, The metachromatic staining reaction, J. Histochem. Cytochem. 3 (1955) 227–237.
[17] R.W. Horobin, How Romanowsky stains work and why they remain valuable – including a proposed universal Romanowsky staining mechanism and a rational troubleshooting scheme, Biotech. Histochem. 86 (2011) 36–51.
[18] W.J. Williams, E. Larson, T.L. Phillips, A neoplastic connective tissue mast cell capable of continuous growth in tissue culture, J. Biophys. Biochem. Cytol. 6 (1959) 361–368.
[19] E.B. Hunziker, A. Ludi, W. Herrmann, Preservation of cartilage matrix proteoglycans using cationic dyes chemically related to ruthenium hexaammine trichloride, J. Histochem. Cytochem. 40 (1992) 909–917.
[20] J.A. Szirmai, Quantitative approaches in histochemistry of mucopolysaccharides, J. Histochem. Cytochem. 11 (1963) 24.
[21] T. Wittenborn, T. Nielsen, J.V. Nygaard, E.K. Larsen, T. Thim, L.M. Rydtoft, T. Vorup-Jensen, J. Kjems, N.C. Nielsen, M.R. Horsman, E. Falk, Ultrahigh-field DCE-MRI of angiogenesis in a novel angiogenesis mouse model, J. Magn. Reson. Imaging 35 (2012) 703–710.
[22] H. Brix, J.E. Lyngby, H.-H. Schierup, Eelgrass (*Zostera marina* L.) as an indicator organism of trace metals in the Limfjord, Denmark, Mar. Environ. Res. 8 (1983) 165–181.
[23] M.O. Andersen, J.V. Nygaard, J.S. Burns, M.K. Raarup, J.R. Nyengaard, C. Bunger, F. Besenbacher, K.A. Howard, M. Kassem, J. Kjems, SiRNA nanoparticle functionalization of nanostructured scaffolds enables controlled multilineage differentiation of stem cells, Mol. Ther. 18 (2010) 2018–2027.
[24] M.F. Casula, P. Floris, C. Innocenti, A. Lascialfari, M. Marinone, M. Corti, R.A. Sperling, W.J. Parak, C. Sangregorio, Magnetic resonance imaging contrast agents based on iron oxide superparamagnetic ferrofluids, Chem. Mater. 22 (2010) 1739–1748.
[25] D.E. Owens 3rd, N.A. Peppas, Opsonization, biodistribution, and pharmacokinetics of polymeric nanoparticles, Int. J. Pharm. 307 (2006) 93–102.
[26] M. Roser, D. Fischer, T. Kissel, Surface-modified biodegradable albumin nano- and microspheres. II: Effect of surface charges on in vitro phagocytosis and biodistribution in rats, Eur. J. Pharm. Biopharm. 46 (1998) 255–263.
[27] M. Gaumet, A. Vargas, R. Gurny, F. Delie, Nanoparticles for drug delivery: the need for precision in reporting particle size parameters, Eur. J. Pharm. Biopharm. 69 (2008) 1–9.
[28] R. Gref, M. Luck, P. Quellec, M. Marchand, E. Dellacherie, S. Harnisch, T. Blunk, R.H. Muller, 'Stealth' corona-core nanoparticles surface modified by polyethylene glycol (PEG): influences of the corona (PEG chain length and surface density) and of the core composition on phagocytic uptake and plasma protein adsorption, Colloids Surf. B Biointerfaces 18 (2000) 301–313.
[29] W.J. Mulder, G.J. Strijkers, K. Nicolay, A.W. Griffioen, Quantum dots for multimodal molecular imaging of angiogenesis, Angiogenesis 13 (2010) 131–134.
[30] G.J. Strijkers, E. Kluza, G.A. Van Tilborg, D.W. van der Schaft, A.W. Griffioen, W.J. Mulder, K. Nicolay, Paramagnetic and fluorescent liposomes for target-specific imaging and therapy of tumor angiogenesis, Angiogenesis 13 (2010) 161–173.
[31] D.B. Ellegala, H. Leong-Poi, J.E. Carpenter, A.L. Klibanov, S. Kaul, M.E. Shaffrey, J. Sklenar, J.R. Lindner, Imaging tumor angiogenesis with contrast ultrasound and microbubbles targeted to alpha(v)beta3, Circulation 108 (2003) 336–341.
[32] H. Leong-Poi, J. Christiansen, A.L. Klibanov, S. Kaul, J.R. Lindner, Noninvasive assessment of angiogenesis by ultrasound and microbubbles targeted to alpha(v)-integrins, Circulation 107 (2003) 455–460.

[33] W. Cai, X. Chen, Multimodality molecular imaging of tumor angiogenesis, J. Nucl. Med. 49 (Suppl. 2) (2008) 113S–128S.
[34] R. Haubner, A.J. Beer, H. Wang, X. Chen, Positron emission tomography tracers for imaging angiogenesis, Eur. J. Nucl. Med. Mol. Imaging 37 (Suppl. 1) (2010) S86–103.
[35] A.Z. Wang, F. Gu, L. Zhang, J.M. Chan, A. Radovic-Moreno, M.R. Shaikh, O.C. Farokhzad, Biofunctionalized targeted nanoparticles for therapeutic applications, Expert Opin. Biol. Ther. 8 (2008) 1063–1070.
[36] D.B. Kirpotin, D.C. Drummond, Y. Shao, M.R. Shalaby, K. Hong, U.B. Nielsen, J.D. Marks, C.C. Benz, J.W. Park, Antibody targeting of long-circulating lipidic nanoparticles does not increase tumor localization but does increase internalization in animal models, Cancer Res. 66 (2006) 6732–6740.
[37] K.F. Pirollo, E.H. Chang, Does a targeting ligand influence nanoparticle tumor localization or uptake?, Trends Biotechnol 26 (2008) 552–558.
[38] N. Kamaly, T. Kalber, M. Thanou, J.D. Bell, A.D. Miller, Folate receptor targeted bimodal liposomes for tumor magnetic resonance imaging, Bioconjug. Chem. 20 (2009) 648–655.
[39] Y. Matsumura, H. Maeda, A new concept for macromolecular therapeutics in cancer chemotherapy: mechanism of tumoritropic accumulation of proteins and the antitumor agent smancs, Cancer Res. 46 (1986) 6387–6392.